

Lipid droplets as substrates for protein phase separation

Advika Kamatar, ¹ Jack P. K. Bravo, ² Feng Yuan, ¹ Liping Wang, ³ Eileen M. Lafer, ³ David W. Taylor, ^{2,4,5,6} Jeanne C. Stachowiak, ^{1,7,*} and Sapun H. Parekh^{1,*}

¹Department of Biomedical Engineering, University of Texas at Austin, Austin, Texas; ²Department of Molecular Biosciences, University of Texas at Austin, Austin, Texas; ³Department of Biochemistry and Structural Biology, University of Texas Health Science Center at San Antonio, San Antonio, Texas; ⁴Interdisciplinary Life Sciences Graduate Program, University of Texas at Austin, Austin, Texas; ⁵Center for Systems and Synthetic Biology, University of Texas at Austin, Austin, Texas; ⁶LIVESTRONG Cancer Institutes, Dell Medical School, Austin, Texas; and ⁷McKetta Department of Chemical Engineering, University of Texas at Austin, Austin, Texas

ABSTRACT Membrane-associated protein phase separation plays critical roles in cell biology, driving essential cellular phenomena from immune signaling to membrane traffic. Importantly, by reducing dimensionality from three to two dimensions, lipid bilayers can nucleate phase separation at far lower concentrations compared with those required for phase separation in solution. How might other intracellular lipid substrates, such as lipid droplets, contribute to nucleation of phase separation? Distinct from bilayer membranes, lipid droplets consist of a phospholipid monolayer surrounding a core of neutral lipids, and they are energy storage organelles that protect cells from lipotoxicity and oxidative stress. Here, we show that intrinsically disordered proteins can undergo phase separation on the surface of synthetic and cell-derived lipid droplets. Specifically, we find that the model disordered domains FUS LC and LAF-1 RGG separate into protein-rich and protein-depleted phases on the surfaces of lipid droplets. Owing to the hydrophobic nature of interactions between FUS LC proteins, increasing ionic strength drives an increase in its phase separation on droplet surfaces. The opposite is true for LAF-1 RGG, owing to the electrostatic nature of its interprotein interactions. In both cases, protein-rich phases on the surfaces of synthetic and cell-derived lipid droplets demonstrate molecular mobility indicative of a liquid-like state. Our results show that lipid droplets can nucleate protein condensates, suggesting that protein phase separation could be key in organizing biological processes involving lipid droplets.

SIGNIFICANCE Membrane-associated liquid protein networks play important roles throughout the cell, from signal transduction to endocytosis. Could other cellular lipid substrates orchestrate protein condensation? Lipid droplets are ubiquitous intracellular reservoirs of neutral lipids that help maintain energy homeostasis and facilitate communication between other organelles. However, many processes within lipid droplet biology are not fully understood. Here, we show that a condensed protein network can form on the surfaces of synthetic and cell-derived lipid droplets, and that these condensates demonstrate liquid-like properties, including molecular mobility and merging and re-rounding. The ability of cell-derived lipid droplets to nucleate protein condensates suggests that protein phase separation may play a role in organizing the surfaces of lipid droplets.

INTRODUCTION

Protein phase separation or condensation is the process by which proteins in solution self-assemble into a protein-dense phase by forming a network of weak, multivalent interactions (1). This process results in partitioning of proteins into a protein-rich phase and a protein-depleted phase. Under appropriate stimuli, including temperature, pH, ionic

can behave like a liquid, such that droplets of this phase can coalesce, fuse, and undergo rapid molecular exchange with the protein-depleted phase (2). When the protein dense phase has the properties of a liquid, the assembly of condensates is referred to as liquid-liquid phase separation (LLPS). This process underlies the formation of membrane-less organelles like nucleoli, stress granules, and centrosomes, and is thus crucial for intracellular organization (3).

strength, and protein concentration, the protein-dense phase

Recent work has shown that protein interaction with lipid membranes can induce condensation at substantially lower concentrations than would occur if proteins were free in

 $Submitted\ November\ 21,\ 2023,\ and\ accepted\ for\ publication\ March\ 7,\ 2024.$

*Correspondence: jcstach@austin.utexas.edu or sparekh@utexas.edu

Editor: Galia Debelouchina.

https://doi.org/10.1016/j.bpj.2024.03.015

© 2024 Biophysical Society.



solution (4–7). For example, the A. gossypii protein Whi3 forms droplets at micromolar protein concentrations and nonphysiological salt concentrations in vitro (8). However, upon membrane recruitment, 50 nM Whi3 is sufficient to form condensates at physiological salt concentrations, suggesting that membranes reduce the protein concentration necessary for condensation (4). Similarly, the endocytic proteins Fcho1 and Eps15 coassemble into two-dimensional condensates at concentrations of 100 nM on flat lipid multibilayers, whereas 3 µM of Eps15 and 125 nM of Fcho1 is required for threedimensional droplet formation (5). For non-his-tagged FUS LC, nonspecific interactions with negatively charged lipids were enough to trigger condensation at 10 μ M (6); in the absence of lipids, no phase separation was observed at room temperature until $\sim 200 \, \mu \text{M}$ (9). This lipid-induced change in the critical concentration required for condensation is important because the cytosol of the cell is densely populated by membrane-bound compartments, from organelles to trafficking vesicles (10). Therefore, lipid bilayers provide abundant substrates upon which condensation, either solid- or liquid-like, could occur. For example, recent work has shown that formation of a liquid-like protein assembly at the plasma membrane is critical for productive endocytic events (5), and LLPS on giant unilamellar vesicles has been shown to drive membrane bending, suggesting that condensates could contribute to diverse membrane protrusions (11). Furthermore, membrane-associated LLPS seems to be a broadly observed mechanism by which cells can organize complex processes at the membrane, including the force-dependent assembly of focal adhesions (12) and actin polymerization (13), synaptic vesicle clustering (14), synaptogenesis (15,16), and T cell receptor signal transduction (17).

In addition to bilayer membranes, lipid droplets (LDs) are also ubiquitous lipid substrates found in the cytoplasm of most cell types. A lipid bilayer is composed of two leaflets of amphipathic lipids with the hydrophilic headgroups oriented toward the aqueous environment and the hydrophobic tails pointed inward toward each other. In contrast, an LD is composed of an amphipathic phospholipid monolayer surrounding a hydrophobic core composed of neutral lipids, including triacylglycerols (TAGs), sterol esters, and retinyl esters (18). LDs often have proteins embedded at the phospholipid surface, including the perilipin family (PLIN1-5), membrane trafficking proteins like Rabs, SNAREs, and Arfs, and proteins involved in protein degradation (19). While first understood as energy storage sites, in the past three decades, it has become clear that LDs are dynamic organelles with important roles in energy homeostasis, cellular communication, and disease (18). If condensation helps to organize proteins on the surfaces of lipid bilayers, could it also occur on the surfaces of LDs? If so, it could provide a mechanism for organizing key events in LD biogenesis and function. Indeed, condensation of Cidec, an LD-binding protein with a crucial role in LD fusion in white adipose tissue, has been observed at LD-LD contact sites, and its ability to condense was essential for the maintenance of LD size and lipid exchange across the contact site (20). However, Lyu and colleagues observe condensates only at LD-LD contact sites; even after replacing the native N-terminal amino acids 1–135 with the intrinsically disordered region (IDR) of hnRNPDL, a domain which is known to drive phase separation, they did not observe condensates on the monolayer regions of an LD outside of the contact sites. Thus, we wondered whether a single lipid monolayer is a viable substrate for two-dimensional phase separation, or whether there is an intrinsic biophysical feature of lipid monolayers that prohibits associated phase separation.

Therefore, we investigated the extent to which LDs can provide a substrate for LLPS of proteins. Specifically, we characterized the condensation of well-studied proteins involved in LLPS on the surfaces of synthetic and cell-derived LDs. We found that at various salt concentrations, the low complexity domain of fused in sarcoma (FUS LC) and the RGG domain of LAF-1 (RGG), followed opposing trends in their tendency to condense on the LD surface, in line with the current understanding of the intermolecular interactions driving their condensation. Furthermore, we found that these protein condensates remain liquid-like on the surface of both synthetic and cell-derived LDs. Our findings indicate that LLPS is a viable mechanism for protein organization on the LD surface.

MATERIALS AND METHODS

Protein purification

Expression and purification of his-tagged FUS LC, containing an N-terminal 6xHis-tag and amino acids 1-163 of full-length FUS, (his-FUS LC) was carried out exactly as described by Yuan et al., including starting plasmids (11). In brief, his-FUS LC was overexpressed in E. coli BL21(DE3) cells. One-liter cultures were induced with 1 mM IPTG for 4 h at 37°C and 220 rpm and pellets of cells expressing his-FUS LC were harvested via centrifugation when the OD_{600} reached 0.8. The pellets were then lysed in a buffer containing 0.5 M Tris-HCl (pH 8), 5 mM EDTA, 5% glycerol, 10 mM β-ME, 1 mM PMSF, 1% Triton X-100 and one EDTA-free protease inhibitor tablet (Sigma-Aldrich, St. Louis, MO) for 5 min on ice and then sonicated. The cell lysates were centrifuged at $134,000 \times g$ for 40 min, after which his-FUS LC resided in the insoluble fraction. Therefore, the insoluble fraction was resuspended in a solubilizing buffer of 8 M urea, 20 mM NaPi (pH 7.4), 300 mM NaCl and 10 mM imidazole and centrifuged at 134,000 × g for 40 min. In denaturing conditions, his-FUS LC is ureasoluble and thus resided in the supernatant. This supernatant was then mixed with Ni-NTA resin (G-Biosciences, St. Louis, MO) for 1 h at 4°C, settled in a glass column and washed with the above solubilizing buffer. The bound proteins were eluted from the Ni-NTA resin with a buffer containing 8 M urea, 20 mM NaPi (pH 7.4), 300 mM NaCl and 500 mM imidazole. In this preparation, the TEV-cleavable his-tag of this protein was not removed, as it was needed for membrane binding via interaction with DGS-NTA(Ni) lipids. The purified proteins were then buffer exchanged into 20 mM CAPS (pH 11) storage buffer using 3K Amicon Ultra centrifugal filters (Millipore, St. Louis, MO). Small aliquots of the protein were frozen in liquid nitrogen at a protein concentration of approximately 1 mM.

Expression and purification of his-LAF-1 RGG, containing amino acids 1-168 of LAF-1 and a C-terminal 6xHis tag, was performed exactly as described previously, including starting plasmids (11). In brief,

his-LAF-1 RGG was overexpressed in E. coli BL21(DE3) cells. One-liter cultures were induced with 0.5 mM IPTG overnight at 18°C and 220 rpm, and pellets of cells expressing his-LAF-1 RGG were harvested from the cultures via centrifugation when the OD₆₀₀ reached 0.8. The pellets were then lysed in a buffer containing 20 mM Tris, 500 mM NaCl, 20 mM imidazole, and one EDTA-free protease inhibitor tablet (Sigma-Aldrich) for 5 min on ice and then sonicated. The cell lysates were centrifuged at $134,000 \times g$ for 40 min, after which his-LAF-1 RGG resided in the supernatant. The supernatant was then mixed with Ni-NTA resin (G-Biosciences) for 1 h, settled in a glass column, and washed with a buffer containing 20 mM Tris, 500 mM NaCl, 20 mM imidazole (pH 7.5). The bound proteins were eluted from the Ni-NTA resin with a buffer containing 20 mM Tris, 500 mM NaCl, 500 mM imidazole (pH 7.5). The purified proteins were then buffer exchanged into 20 mM Tris, 500 mM NaCl (pH 7.5) using Amicon Ultra centrifugal filters. Small aliquots of the protein were frozen in liquid nitrogen at a protein concentration of approximately 120 μ M and stored at -80° C. To promote solubility of the LAF-1 RGG protein, the entire purification process was performed at room temperature, except for the cell lysis process, which was done on ice.

His-clathrin was purified according to a previously published protocol (21). His-GFP and his-mCherry purification were performed according to a previously published protocol (22).

Protein labeling

His-FUS LC was labeled with Atto-488 or Atto-647 NHS-ester fluorescent dyes (ATTO-TEC, Siegen, Germany and Sigma-Aldrich). Labeling occurred at or near the N-terminus because only the N-terminus and a lysine at residue position 5 in the leader sequence preceding the N-terminal region hexa-histidine tag were expected to react with the NHS-functionalized dye. The labeling reaction took place in a 50 mM HEPES buffer (pH 7.4). Dye was added to the protein in twofold stoichiometric excess and allowed to react for 30 min at room temperature, empirically resulting in a labeling ratio near 1:1 dye/protein. Labeled protein was then buffer exchanged into 20 mM CAPS (pH 11) buffer and separated from unconjugated dye using 3K Amicon columns (MilliporeSigma, Burlington, MA). His-LAF-1 RGG was labeled with Atto-488 in its storage buffer (20 mM Tris, 500 mM NaCl [pH 7.5]). Protein and dye concentrations were monitored using UVvis spectroscopy using a molar extinction coefficient of 35,760 cm⁻¹ for FUS LC and 16,390 cm⁻¹ for RGG. Labeled proteins were dispensed into small aliquots, flash frozen in liquid nitrogen and stored at -80°C. His-clathrin was labeled with Atto594 NHS-ester (ATTO-TEC and Sigma-Aldrich) according to a previously published protocol (21) and was ultracentrifuged and used immediately after labeling to minimize aggregation.

Labeled protein was mixed with unlabeled protein (if necessary) to achieve a 10% labeled protein stock for use in all imaging experiments.

Preparation of synthetic LDs

1,2-Dioleoyl-sn-glycero-3-phosphocholine (DOPC), 1,2-dioleoyl-sn-glycero-3-phospho-(1'-rac-glycerol) (sodium salt), L-α-phosphatidylcholine (Egg PC), 1,2-dioleoyl-sn-glycero-3-[(N-(5-amino-1-carboxypentyl)iminodiacetic acid)succinyl] (nickel salt) (18:1 DGS-NTA(Ni)), and 1,2-dioleoylsn-glycero-3-phosphoethanolamine-N-(cap biotinyl) (sodium salt) (18:1 Biotinyl Cap PE) were purchased from Avanti Polar Lipids (Alabaster, AL). Texas Red-DHPE was purchased from AAT Bioquest (Pleasanton, CA). All lipid stocks were stored at -80° C.

Glass vials were cleaned by washing with acetone, then with Neutrad (Thermo Fisher Scientific, Waltham, MA), and rinsing with ultrapure H₂O. Lipid mixtures dissolved in chloroform were mixed in the appropriate molar ratios in the clean glass vial to obtain 1.60×10^{-7} mol of lipid. Ten microliters of olive oil was added to the lipid mixture and gently shaken to mix before the chloroform was evaporated under a stream of N₂. The lipids were further dried in a vacuum desiccator for at least 2 h to remove all solvent. Lipids and olive oil were then heated at 37°C for 10 min and vortexed for 10 s to evenly mix the lipids within the olive oil. The lipid mixture was resuspended in 25 mM HEPES, 150 mM NaCl (pH 7.4) and vortexed 3 times for 10 s to generate an emulsion of LDs suspended in aqueous buffer. LDs were stored at 4°C and used within 1 day of formation.

Preparation of GUVs

Giant unilamellar vesicles (GUVs) were prepared as previously reported using electroformation (11). Lipid mixtures dissolved in chloroform were combined in a glass vial washed with acetone and Neutrad and rinsed with ultrapure H_2O to obtain 2.0×10^{-7} mol of lipid. The lipid mixture was spread into a film on acetone- and Neutrad-cleaned indium-tin-oxide-coated glass slides (resistance \sim 8-12W sq⁻¹) and further dried in a vacuum desiccator for at least 2 h to remove all the solvent. Electroformation was performed at 55°C in 340 milliosmole glucose solution. The voltage was increased every 3 min from 50 to 1400 mVpp for the first 30 min at a frequency of 10 Hz. The voltage was then held at 1400 mVpp for 120 min and finally was increased to 2200 mVpp for the last 30 min during which the frequency was adjusted to 5 Hz. GUVs were stored at 4°C and used within 2 days after electroformation.

Tethering of synthetic LDs and GUVs

LDs and GUVs were tethered to glass coverslips as described previously (11). In brief, glass coverslips were passivated with a layer of 2% biotinylated PLL-PEG-8 kDa. LDs and GUVs were doped with 2% 18:1 Biotinyl Cap PE (Avanti Polar Lipids) and tethered to the passivated surface using Neutravidin (Thermo Fisher Scientific).

PLL-PEG was synthesized by combining amine reactive PEG and PEGbiotin (Sigma-Aldrich) in molar ratios of 98 and 2%, respectively. This PEG mixture was added to a 20 mg/mL mixture of PLL (Sigma-Aldrich) in 50 mM sodium tetraborate (pH 8.5) such that the molar ratio of lysine subunits to PEG was 5:1. The mixture was continuously stirred at room temperature overnight then buffer exchanged into 25 mM HEPES, 150 mM NaCl (pH 7.4) using Centri-Spin size exclusion columns (Princeton Separations, Monmouth Junction, NJ).

To each 5 mm imaging well, 20 µL of 2% biotinylated PLL-PEG was added and incubated at room temperature for 20 min. Wells were washed with 25 mM HEPES (pH 7.4) containing the NaCl concentration specified for the experiment using gentle pipetting until PLL-PEG reached at least a 1000-fold dilution. Then 4 μL of Neutravidin at a stock concentration of 1 μg/μL dissolved in 25 mM HEPES 150 mM NaCl (pH 7.4) was added to the well, incubated at room temperature for 10 min, and wells were washed with the appropriate buffer to remove excess Neutravidin (1000-fold dilution). LDs or GUVs were diluted in a 1:5 or 1:6 ratio, respectively, added to the well, and incubated for 10-15 min at room temperature. For LDs, the glass slide was turned upside down to facilitate adherence to the treated surface as the LDs tended to rise upward within the aqueous buffer. For GUVs, the well was gently rinsed with the appropriate buffer to remove excess GUVs. For experiments involving protein, protein was then added to the well at the appropriate concentration, and wells were covered with a glass coverslip to prevent evaporation before imaging using confocal microscopy.

Fluorescence microscopy

Imaging experiments were performed using a spinning disc confocal super resolution microscope (SpinSR10, Olympus, Tokyo, Japan) equipped with a 1.49 NA/100× oil immersion objective fitted with a Hamamatsu Orca Flash 4.0V3 scientific complementary metal-oxide-semiconductor digital camera. Laser wavelengths of 488, 561, and 640 nm were used for excitation. For sample preparation, No. 1.5 Glass coverslips were cleaned in 2%, v/v, Hellmanex III solution (Hellma Analytics, Müllheim, Germany), rinsed thoroughly with ultrapure H_2O , and dried with compressed air. Imaging wells were formed by cutting 5-mm holes in PDMS gaskets or 1.5-mm-thick silicone gaskets (Grace Bio-Labs, Bend, OR) using a biopsy punch. Gaskets were cleaned with Neutrad, rinsed with ultrapure H_2O , and dried thoroughly with compressed air before being placed on dry coverslips to create a temporary waterproof seal. A second coverslip was placed on top of the imaging well to seal the chamber and prevent evaporation.

Cryoelectron microscopy

To image the synthetic LDs using cryoelectron microscopy, a diameter of 50–200 nm and an LD high concentration was desired. To achieve size reduction and increased concentration of LDs, 2.46 mg of Egg PC and 14 μ L of olive oil were dried overnight in a vacuum desiccator. Lipids and olive oil were rehydrated in 25 mM HEPES 150 mM NaCl (pH 7.4) by vortexing and tip sonicated on ice for 5 cycles of 1 min on ice. LDs (2.5 μ L) was applied to glow discharged holey carbon grids (Quantifoil 1.2/1.3) (Quantifoil, Großlöbichau, Germany), blotted for 6 s with a blot force of 0 and rapidly plunged into liquid nitrogen-cooled ethane using an FEI Vitrobot MarkIV (Thermo Fisher Scientific). Images were acquired on a FEI Glacios cryo-TEM (Thermo Fisher Scientific) equipped with a Falcon 4 detector with a pixel size of 0.94 Å, and a total exposure time of 15 s resulting in a total accumulated dose of 40 e/Ų which was split into 60 electron-event representation (EER) fractions. Motion correction was performed using crypSPARC (23).

For the quantification of monolayer thickness, the thickness of the dark phospholipid ring was measured using ImageJ. Seventeen LDs were measured at three separate locations for each LD structure for a total of 51 measurements. All 51 measurements were averaged, as shown in Fig. S1 C. For the quantification of bilayer thickness, the total distance across two resolvable phospholipid layers was measured using ImageJ. Twenty vesicles were measured at three separate locations for each vesicle structure, for a total of 60 measurements. All 60 measurements were averaged, as shown in Fig. S1 C.

Phase diagram experiments

For phase diagram experiments involving varying NaCl concentrations, wells were washed, and protein dilutions were made with 25 mM HEPES (pH 7.4) with a NaCl concentration corresponding to the desired final concentration. For his-FUS LC experiments, initial protein dilutions were made in 0.5 mM CAPS 150 mM NaCl (pH 11) to prevent droplet formation in solution. Final protein dilutions before addition to the well were made in 25 mM HEPES with a NaCl concentration that matched the desired NaCl concentration. For his-tagged RGG (his-RGG) experiments, initial protein dilutions were made in 50 mM Tris 500 mM NaCl (pH 7.4) to prevent droplet formation in solution. Final protein dilutions before addition to the well were made in 25 mM HEPES (pH 7.4) with an NaCl concentration adjusted such that the final concentration of the protein dilution matched the desired NaCl concentration. Following protein addition, samples were sealed to prevent evaporation and allowed to incubate for 30 min before imaging. Image stacks taken at fixed distances perpendicular to the coverslip plane were acquired after protein addition. At least 15 fields of views were randomly selected for each sample for further analysis after the addition of protein.

Fluorescence recovery after photobleaching on LDs

For experiments on synthetic LDs, fluorescence recovery after photobleaching was performed on an Olympus Fluoview 3000 confocal microscope with a 1.1 NA/60× water immersion objective and water-matching oil immersion medium (n=1.3310, Cargille Laboratories, Cedar Grove, NJ). Bleaching of a 2.1 μ m diameter region of interest (ROI) was performed us-

ing a 488 nm laser at 75% laser power for 10 s per ROI. Images were acquired every 1.09 s for his-tagged GFP (his-GFP) and every 5 s for his-FUSLC and his-clathrin to capture the dynamics of recovery while minimizing photobleaching. Raw his-GFP and his-FUS LC intensity values for the bleached region were normalized to account for photobleaching using Eq. 1 and stretched to standardize bleach depth using Eq. 2.

$$I_{norm} = \frac{\left(\frac{bleach\ ROI}{bleach\ ROI_{max}}\right)}{\left(\frac{control\ ROI}{control\ ROI_{max}}\right)}$$
(Equation 1)

$$I_{norm\&stretch} = \frac{I_{norm} - I_{norm,min}}{I_{norm,max} - I_{norm,min}}$$
 (Equation 2)

Raw intensity values for the bleached region for his-clathrin were not normalized for photobleaching because while no recovery was observed, photobleaching of the surrounding region caused an artificial rise in recovery using the previous two formulas. Thus, his-clathrin raw intensity values were normalized using Eq. 3 and stretched using Eq. 2.

$$I_{norm} = \frac{bleach \, ROI}{bleach \, ROI_{\text{max}}}$$
 (Equation 3)

Normalized and stretched recovery curves were plotted as a function of time. Average recovery curves for each protein were calculated by averaging the normalized and stretched intensity values for all replicates at each time step.

Calculation of $t_{1/2}$: to calculate $t_{1/2}$ values for his-FUS LC, the data for each replicate was fit to the double-exponential equation of Eq. 4 using the Levenberg-Marquardt method with an initial parameter guess of 1 for each coefficient in MATLAB:

$$y = a * (1 - e^{-b*t}) + c * (1 - e^{-d*t})$$
 (Equation 4)

The equation was solved for the time at which the intensity reached 0.5 using the obtained fit coefficients to calculate $t_{1/2}$.

Because the his-GFP data was noisy and the data reached a plateau of recovery within the timespan of data collection, fitting was not needed to calculate the $t_{1/2}$ values. Instead, the times and intensities immediately before and after the intensity reached 50% of the maximum intensity were used to linearly interpolate the time at which the intensity reached 0.5*(max intensity).

For experiments on cell-derived LDs, fluorescence recovery after photobleaching (FRAP) was performed using the Olympus FRAP unit 405 nm laser and an additional $3.2\times$ magnification lens using 32% laser power.

Mammalian cell culture

Human retinal pigmented epithelial (RPE) cells (ARPE-19) were purchased from American Type Culture Collection (Manassas, VA). RPE cells were cultured in 1:1 F12/DMEM supplemented with 10% FBS, 20 mM HEPES, and 1% penicillin, 1% streptomycin, 1% L-glutamine. Cells were incubated at 37°C with 5% $\rm CO_2$ and passaged every 72–96 h. If cells were incubated for 96 h between passages, media was changed at the 48-h time point.

For fluorescent imaging, cells were seeded in chambered 8-well glass bottom slides (CellVis, Mountain View, CA) at a density of 5000 cells per well. For cells in which LD formation was induced, cell media was changed and a final concentration of 1 mM OA-BSA (oleic acid with bovine serum albumin) was added to culture media for 48 h before imaging. Before imaging, the media was removed, and cells were washed with PBS and incubated in PBS containing 5 μ M Draq5 far-red nuclear stain (Thermo Fisher Scientific)

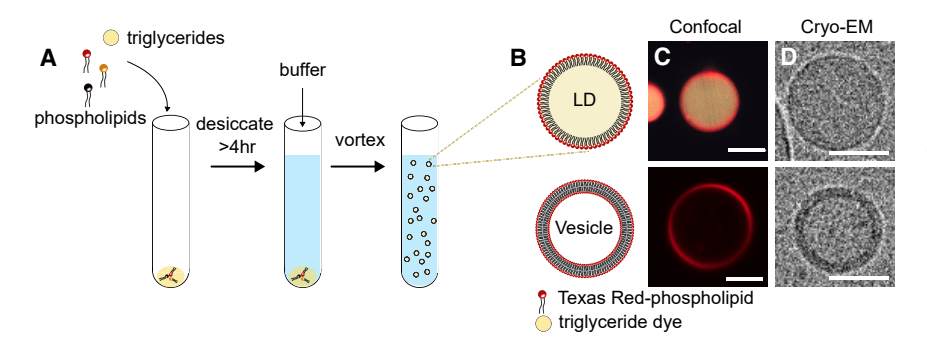


FIGURE 1 LD synthesis and characterization. (A) Schematic of LD synthesis. (B) Schematic of an LD characterized by a monolayer of phospholipids surrounding a core of neutral triacylglycerol (TAG) (upper), and a bilayer vesicle characterized by a phospholipid bilayer surrounding an aqueous core (lower). (C) Confocal images of a representative synthesized LD composed of 98 mol % DOPG, 2 mol % CapBioPE, and 0.1 mol % DHPE-Texas Red with Bodipy 505/515-stained TAG (beige) (upper), and a giant unilamellar vesicle (GUV) of the same phospholipid composition (lower). Scale bars, 5 μ m. (D) Cryoelectron micrographs depicting an LD with a phospholipid

monolayer (upper) and vesicles with a phospholipid bilayer (lower). LDs and vesicles were formed with Egg PC. Scale bars, 10 nm. To see this figure in color, go online.

and 2 μ M Bodipy 505/515 (Thermo Fisher Scientific) or 10 μ M Nile Red (Sigma-Aldrich) neutral lipid stain for 10 min. Cells were washed again with PBS and fresh phenol red-free media was added before imaging.

Isolation of cell-derived LDs

To induce LD formation in RPE cells, OA (Sigma-Aldrich) was complexed to fatty acid-free BSA (Sigma-Aldrich) at a 5:1 M ratio of OA/BSA to form OA-BSA. To prepare a 15 mM stock of OA-BSA, first a 300 mM stock of OA was prepared by dissolving oleic acid in EtOH in a glass scintillation vial. When not in use, OA and stocks were flushed with N2 and kept at -20°C. The appropriate mass of BSA was weighed out and dissolved in cell culture media (1:1 F12/DMEM +10% FBS) warmed to 37°C. The BSA solution was mixed on a stir plate at 37°C for 30 min to ensure dissolution of BSA in the media. After BSA dissolved in warm media, additional media was added to achieve the desired stock concentration of 3 mM BSA. and 300 mM OA was added to the BSA solution for a final OA concentration of 15 mM, yielding a 5:1 ratio of OA/BSA. OA precipitates upon addition to the BSA solution, and dissolution was achieved through stirring overnight at 37 °C at 400 rpm on a stir plate. After OA was dissolved in BSA-containing media, the OA-BSA solution was sterile filtered, aliquoted, and stored at -20° C until use. OA-BSA aliquots were thawed at room temperature and used only once to avoid freeze-thaw cycles. Stock concentrations were calculated such that the final EtOH concentration was 0.5%, v/v, when OA-BSA was added to cells at a final concentration of 1 mM OA.

To induce LD formation in RPE cells, RPE cells were passaged and seeded into a 150 mm round cell culture flask. After 48 h, the culture media was exchanged and 15 mM OA-BSA was added to a final concentration of 1 mM OA. Cells were incubated for an additional 48 h, after which time cells were \sim 90% confluent and LDs were densely packed in the cytoplasm.

LDs were isolated according to a previously published STAR protocol (24), with some modifications. In brief, cells were gently washed with PBS and collected in PBS using a cell scraper. Cells were centrifuged at $500 \times g$ for 10 min at 4°C to pellet cells, and the supernatant was discarded. The cell pellet was resuspended in 2 mL of chilled 20 mM Tris 1 mM EDTA (referred to as HLM buffer) containing 1× Pierce protease inhibitor (Thermo Fisher Scientific) and incubated on ice for 10 min before homogenization using a Dounce homogenizer. Homogenate was centrifuged at $1000 \times g$ for 10 min at 4°C to pellet nuclei and unbroken cells. The supernatant was collected and ultracentrifuged within a sucrose density gradient to concentrate the LDs and separate them from the ER and other cell compartment fractions. To create the sucrose gradient, the 2 mL of supernatant was thoroughly mixed with 1 mL of 60% sucrose in HLM buffer to create a final concentration of 20% sucrose containing the cell homogenate and was added to a clean and dry ultracentrifuge tube. 2.1 mL of 5% sucrose HLM buffer was layered on top carefully, so as not to disturb the lower layer. 1.89 mL of HLM buffer was then carefully layered on top of the 5% sucrose layer for a total volume of 7 mL. The sample was centrifuged at $28,000 \times g$ in an S50-ST swinging bucket rotor (Thermo Fisher Scientific) in a Sorvall MX 150 Plus Micro-Ultracentrifuge (Thermo Fisher Scientific) for 30 min at 4°C to float LDs. After centrifugation, LDs were concentrated at the top of the tube and were collected by pipette for imaging and used within 72 h of isolation.

Cell-derived LD imaging

To image LDs without the exogenous addition of protein, a 2 μ M final concentration of Bodipy 505/515 was added to the solution of LDs and gently mixed before adding to the imaging chamber. The imaging chamber was inverted and incubated for 10 min to facilitate LD adhesion to the clean coverslip surface before the chamber was covered with an additional coverslip to prevent evaporation and cell-derived LDs were imaged.

To enable His-tagged protein binding to the cell-derived LD surface, cellderived LDs were mixed with a 2 mM stock concentration of DGS-NTA(Ni) (Avanti Polar Lipids) dissolved in tetrahydrofuran (THF) for a final concentration of $60 \,\mu\text{M}$ DGS-NTA(Ni) and a final v/v concentration of 3% THF. The volume of DGS-NTA(Ni) added was limited to 3%, v/v, to minimize any possible disruption to the LDs in the presence of an organic solvent. Cellderived LDs were vortexed 5 times for 5-s intervals to facilitate incorporation of DGS-NTA(Ni) into the lipid monolayer, as previously demonstrated with biotinylated lipids and giant plasma membrane-derived vesicles (25). Ni-NTA-doped cell-derived LDs were added to the imaging chamber and the chamber was inverted and incubated for 10 min. Then the chamber was washed gently 3 times with 60 µL of 25 mM HEPES to remove excess THF and unincorporated DGS-NTA(Ni). To facilitate faster diffusion and protein mixing, protein was first diluted with buffer (25 mM HEPES [pH 7.4] at 150 mM NaCl for FUS LC and mCherry or 137 mM NaCl for RGG) outside of the imaging chamber to achieve a larger volume of protein, then added to the imaging chamber to achieve the desired final concentration. Protein was gently mixed upon addition to the chamber and the chamber was sealed with an additional coverslip to prevent evaporation during imaging.

RESULTS

Formation and characterization of synthetic LDs

Synthetic LDs were produced according to previously published protocols (26,27), with several modifications. In brief, phospholipids were added to neutral TAGs, and the solvent was evaporated by drying with N2. The phospholipid-oil mixture was heated to 37°C and vortexed to resuspend dried phospholipids in the oil phase. Then, an aqueous buffer was added, and the solution was vortexed to create an emulsion of phospholipid-coated LDs in the aqueous buffer (Fig. 1, A and B). To confirm that the resulting lipid

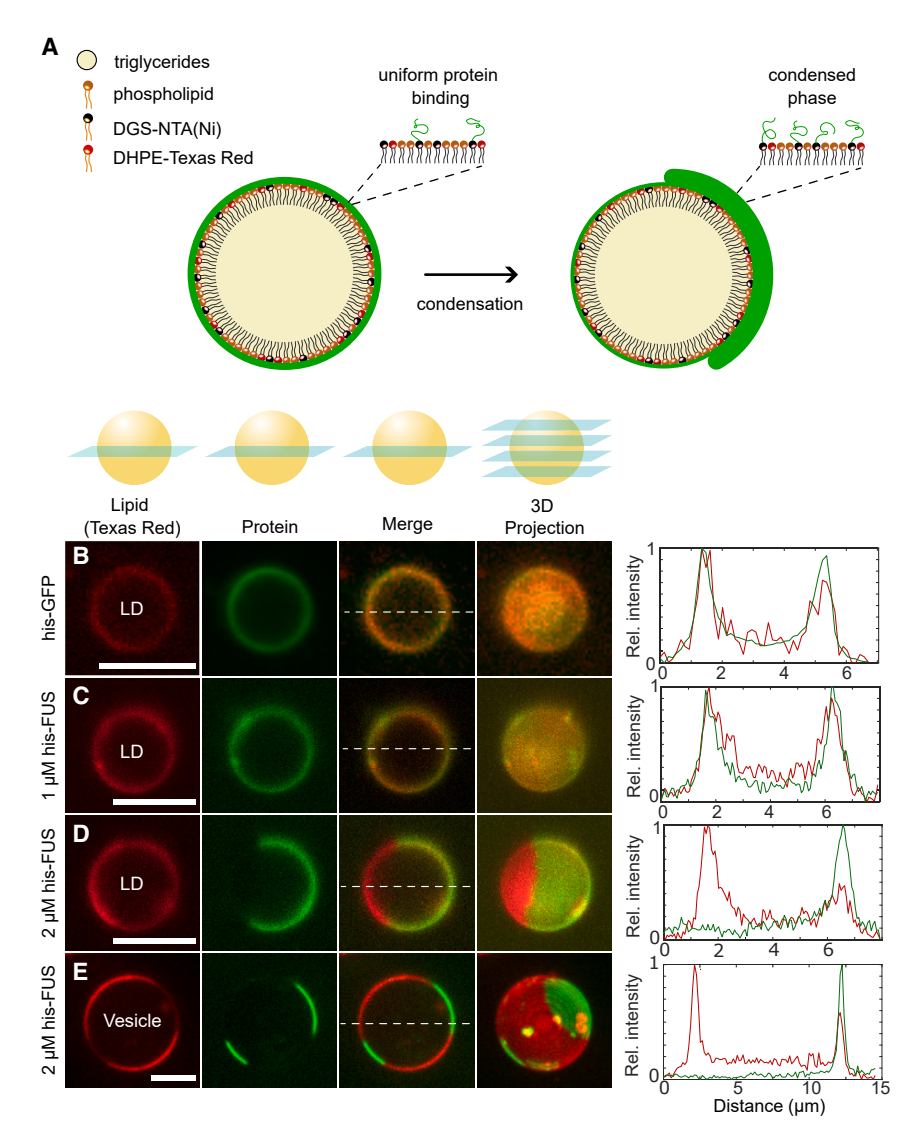


FIGURE 2 Condensation of FUS LC on the surfaces of synthetic LDs. (A) Pictorial representation of a uniform protein coat (left) and a condensed protein coat (right) on the LD phospholipid monolayer. Black lipid headgroups represent DGS-NTA(Ni). Red headgroups represent DHPE-Texas Red. Green lines represent his-tagged proteins. (B-E) Representative confocal images (lipid, protein, and merged channels) and corresponding maximum intensity Z-projections of LDs (B-D) or GUVs (E) incubated with the indicated protein in 25 mM HEPES 150 mM NaCl buffer (pH 7.4). The phospholipid composition was 83 mol % DOPC, 15 mol % DGS-NTA(Ni), 2 mol % CapBioPE, and 0.1 mol % DHPE-Texas Red. (B) LDs were incubated with 2 μM his-GFP, which binds uniformly to the LD surface. (C) LDs were incubated with 1 μ M his-FUS LC, which covers the LD surface uniformly. (D and E) LDs (D) or GUVs (E) were incubated with 2 μM Atto488-labeled FUS LC, which exhibits protein phase separation on the phospholipid surface. Line profiles depict relative fluorescence intensity of the protein and lipid channels at the locations indicated by the corresponding white dashed lines in (B-E), normalized to the maximum intensity values and then stretched between the maximum and minimum intensity values. Red lines indicate the intensity of the lipid channel and green lines indicate the intensity of the protein channel. Scale bars, 5 μ m. To see this figure in color, go online.

substrates had the same structure as a cellular LD, we doped the phospholipids with 0.1 mol % Texas Red-DHPE and added Bodipy 505/515, a neutral lipid dye, and observed the respective localization of the dyed substrates using confocal fluorescence microscopy. As expected, in individual confocal slices, we observed a phospholipid ring surrounding a neutral lipid core (Fig. 1 C, upper panel) in contrast to vesicles with a phospholipid bilayer surrounding an aqueous core (Fig. 1 C, lower panel). To further investigate whether the phospholipid layer was truly a monolayer, as is characteristic of cellular LDs, we performed cryoelectron microscopy to visualize the LD structure at the molecular level. Electron micrographs revealed that the LDs were composed of a monolayer of phospholipids (Fig. 1 D, upper panel) in contrast to vesicles that show two visible layers with a total thickness of approximately 5 nm, in good agreement with the thickness of DOPC vesicles previously reported (28,29) (Fig. 1 D, lower panel; Fig. S1).

Condensation of his-FUS LC on the surfaces of synthetic LDs

We next asked whether LDs could act as a surface to catalyze protein phase separation in a similar manner to bilayer surfaces (Fig. 2 A). To answer this question, we added N-terminal histidine-tagged proteins to synthetic LDs composed of 83 mol % DOPC, 15 mol % DGS-NTA(Ni), 2 mol % Cap Biotin PE, and 0.1 mol % Texas Red-DHPE and observed their organization upon binding. In our system, DGS-NTA(Ni) was used to recruit different hexahistidine-tagged purified proteins to lipid surfaces to study protein phase separation. While NiNTA-His interactions are an artificial approximation of protein binding to LDs, the properties of protein attachment generally resemble attachment via amphipathic helices or hydrophobic helical domains in terms of binding strength (30,31), mobility (32–34), and the presence of distinct domains for membrane binding versus protein-protein interactions

(20,35). Without a His-tag, proteins did not adhere nonspecifically to the synthetic LD surface (Fig. S2). To test our ability to recruit His-tagged proteins to the surface of our LDs, we added his-GFP, a protein that does not undergo LLPS, to the LDs. His-GFP covered the surface of the LDs homogeneously (Fig. 2 B). Next, we asked how model phase-separating proteins might behave on the LD surface. FUS LC is the low complexity domain of FUS, a wellcharacterized phase separating protein region that is rich in glutamine, serine, glycine, and tyrosine amino acids. To visualize protein binding, his-FUS LC was labeled with an NHS-ester-reactive ATTO 488 dye on the N-terminus, and samples were imaged under multichannel confocal microscopy. At a his-FUS LC concentration of 1 μ M, a uniform distribution of protein was observed across the surface of the LD (Fig. 2 C). When the concentration of his-FUS LC was raised to 2 μ M, we observed segregation of the protein into bright and dim regions on the surfaces of LDs (Fig. 2 D). Maximum intensity projections of confocal image stacks showed that FUS LC forms round "caps" that are enriched in protein and are surrounded by regions of significantly lower protein intensity (Fig. 2 D, rightmost image). The difference between homogeneously bound his-GFP and the binding pattern of his-FUS LC suggests that the intensity variation of FUS LC on the LD surface was not due to phospholipid heterogeneity but rather protein phase separation.

Phase separation of FUS LC on the surfaces of LDs appeared morphologically similar to the phase separation of FUS LC on the surfaces of GUVs of a similar composition (Fig. 2 E), which was previously observed (11), suggesting that protein phase separation can occur on both lipid bilayers and monolayers. Curiously, despite morphological similarities, the phase separation effect appears to be weaker on the LD surface than the GUV surface. At low FUS LC concentrations where LLPS was observed on GUVs, no LLPS was observed on the surface of LDs (Fig. S3). It is possible that the weaker LLPS behavior on the LD is due to the less dense lipid packing between a lipid monolayer and a lipid bilayer of the same composition (36,37). For lipid-tethered proteins like a NiNTA-His system, the less densely packed monolayer may have a decreased probability of interaction between two lipid-tethered proteins and fewer overall protein-recruiting lipids for substrates of a similar size, and thus a weaker phase separation effect on a monolayer when compared with a bilayer over the same timescale. We also observed a depletion of the fluorescent lipid in regions of protein condensation on both LDs and GUVs, which could be due to a higher local fraction of DGS-NTA(Ni) in those regions. As the local concentration of protein increases in the dense phase of the condensate, the relative fraction of the protein-bound lipid will likely increase and correspondingly decrease the relative proportion of other lipids, including the fluorescently tagged Texas Red-DHPE.

His-FUS LC condensates on the surfaces of LDs are liquid-like

The boundaries between the protein-poor and protein-rich phases observed in Fig. 2 appear circular, which suggests that the shape of the protein phase is controlled by surface tension, a hallmark of liquids (38,39). To further investigate whether the protein-rich phase formed a liquid-like state, we probed whether FUS LC domains demonstrated additional properties characteristic of liquids, such as merging, re-rounding, and rapid molecular exchange. To observe whether FUS LC domains underwent merging on the LD surface, we imaged LDs immediately after adding protein to the LDs, before protein binding had time to equilibrate. We observed an initially uniform distribution of protein that, within seconds, developed into distinct, rounded, protein-poor regions (Fig. 3 A, dark regions) surrounded by a protein-enriched continuous phase. Once these domains grew large enough to be optically resolved, we observed their rapid movement across the LD surface. When two protein-poor domains came into contact, we observed their fusion, followed by re-rounding of the newly formed, larger protein-poor domain within tens of seconds (Fig. 3 B) another hallmark of liquids.

In addition to merging and re-rounding, liquids often exhibit rapid molecular exchange. We probed the molecular mobility of FUS LC domains on LD surfaces using FRAP. Liquid-like assemblies are formed by a network of weak, multivalent interactions. Therefore, we expected that a liquid-like protein assembly would recover more quickly than a solid-like protein assembly, but more slowly than unassembled proteins that have minimal intermolecular interactions. To test whether protein-rich domains consisting of FUS LC exhibited this intermediate recovery timescale, we compared the recovery profiles of his-FUS LC with his-clathrin and his-GFP. Clathrin, an endocytic coat protein, polymerizes to form a solid-like polyhedral lattice cage (40). In contrast, GFP, which contained the A206K mutation to prevent dimerization (41-43), is a well-structured protein that should diffuse across the LD surface with minimal self-interactions (44). As expected, GFP recovered rapidly after photobleaching (Fig. 3 C), with a $t_{1/2}$ of 4.3 \pm 1.0 s (Fig. 3 D), while clathrin showed essentially no recovery (Fig. 3, C and E). In contrast, the FUS LC domain exhibited an intermediate recovery rate (Fig. 3, C and E), with a $t_{1/2}$ of 119 ± 39 s (Fig. 3 D).

LLPS of his-FUS LC on LDs is driven by increasing salt and protein concentrations

We next investigated whether LLPS on the surfaces of LDs behaves similarly to LLPS of FUS LC in solution (9). Specifically, we mapped the propensity for phase separation on LDs as a function of protein and salt concentration. FUS LC is rich in the amino acids glutamine, glycine, serine, and

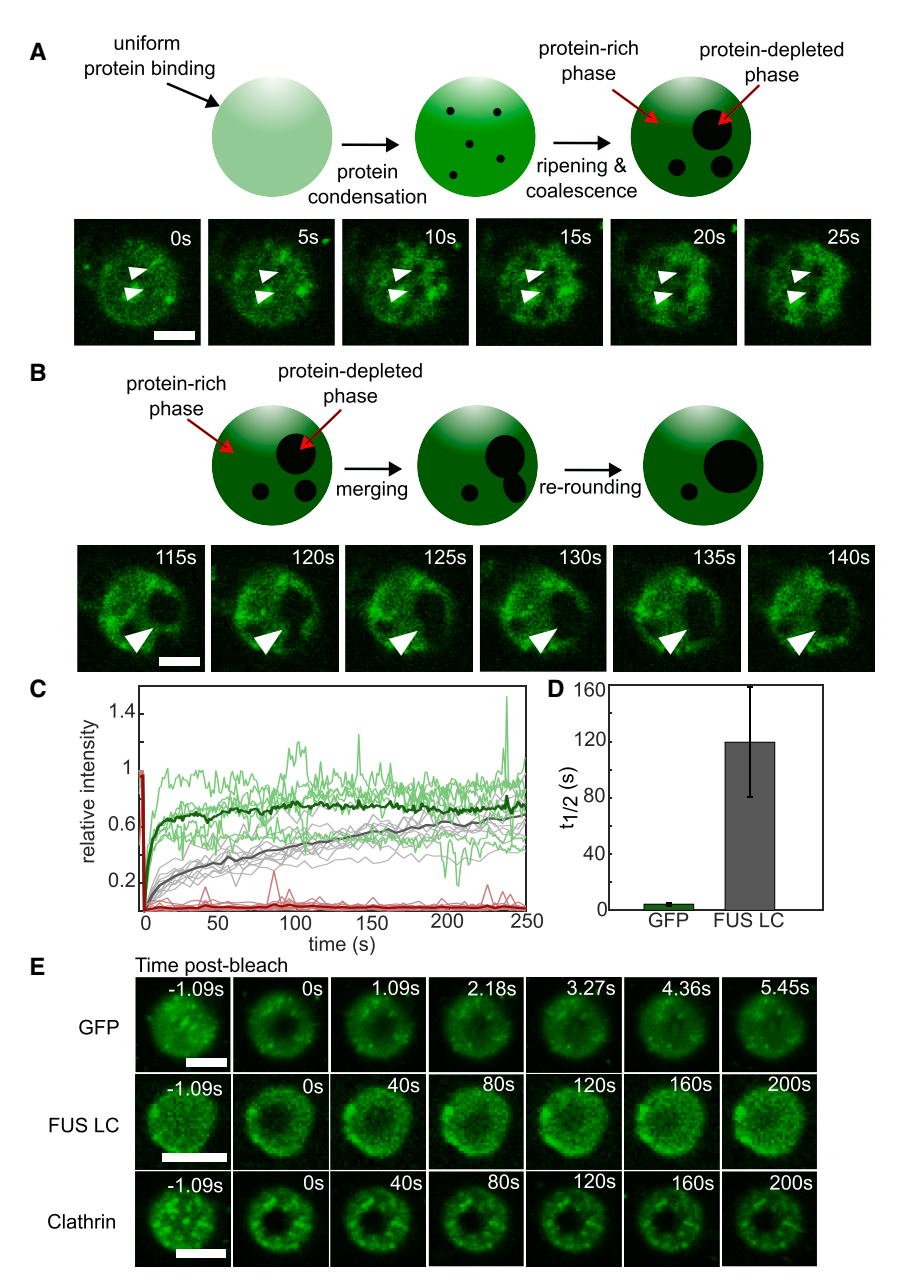


FIGURE 3 Condensates of FUS LC on the surfaces of LDs are liquid-like. (A) Top: pictorial representation of the time-dependent emergence of resolvable protein-depleted regions surrounded by a protein-rich continuous phase. Bottom: confocal image series of the emergence of protein-depleted regions on the surface of an LD. White arrows indicate representative regions where protein depletion occurs. Scale bar, 5 µm. (B) Top: pictorial representation of merging and re-rounding of proteindepleted regions on the LD surface. Bottom: confocal image series of protein-depleted regions merging and re-rounding over time. Scale bar, 5 μm. (C) FRAP recovery profile after photobleaching a 2.1 µm diameter ROI on LDs. Curves in green represent his-GFP. Curves in gray represent his-FUS LC. Curves in red represent his-clathrin. Curves in bold indicate the average recovery curve for the corresponding data sets. (D) $t_{1/2}$ extracted from the recovery curves for his-GFP (4.28 ± 1.01 s) and his-FUS LC (119.48 \pm 39.03 s). $t_{1/2}$ was not calculated for his-clathrin because essentially no recovery was observed. Data represent mean \pm SD (n = 7LDs for GFP, n = 9 LDs for his-FUS LC, outliers were excluded). (E) Image series of fluorescence recovery of LDs covered with his-GFP, his-FUS LC, and his-clathrin protein. Experiments were conducted in 25 mM HEPES, 150 mM NaCl buffer (pH 7.4). Scale bars, 5 μ m. To see this figure in color, go online.

tyrosine, and condensation is driven primarily by hydrogen bonding, π -sp² stacking, π - π , and hydrophobic interactions (9,45). As the ionic strength of the solution increases, we expect hydrophobic interactions to become more dominant, driving LLPS of FUS LC on the surfaces of LDs (Fig. 4 A). All quantifications were made for images collected after 30 min of incubation of LDs with protein, followed by 12–15 min of imaging. For each salt and protein condition, we observed and categorized three phenotypes of protein binding to LDs: uniform binding, segregation of protein into multiple small domains, and full phase separation into a single, larger protein-rich domain (Fig. 4 B). We observed that, as both protein and NaCl concentration increased, the number of LDs with resolvable phase separation increased, in line with previously observed trends (9) (Fig. 4 C).

LLPS of his-RGG is screened by increasing ionic strength

To determine whether the ability to undergo LLPS on LD surfaces was unique to FUS LC or could be more universally applicable to other phase-separating proteins, we next tested an additional, well-studied model LLPS protein, which has distinct physicochemical properties relative to FUS LC. Specifically, we studied the RGG domain of LAF-1, a DDX3 RNA helicase found in the P granules

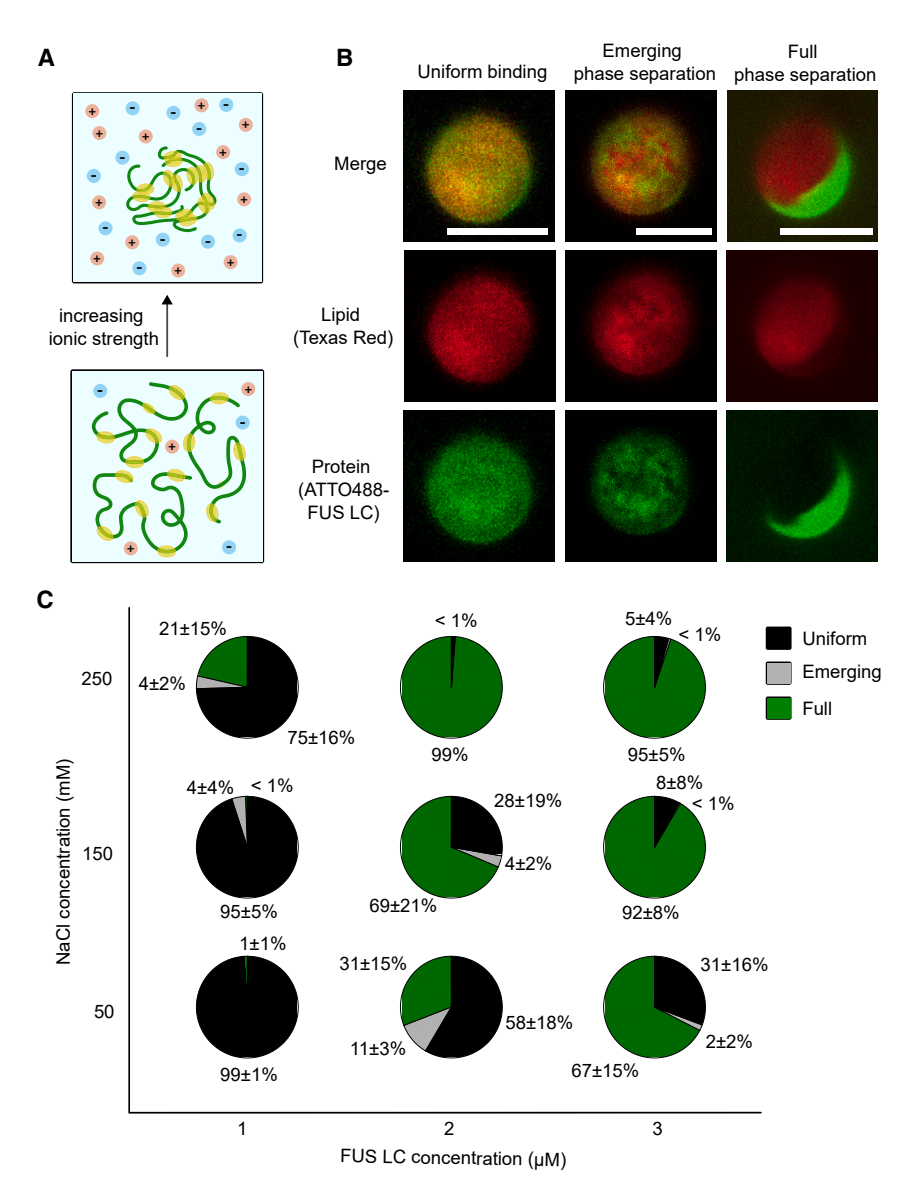


FIGURE 4 LLPS of his-FUS LC on LDs is driven by increasing salt and protein concentrations. (A) Schematic depicting the predicted tendency of his-FUS LC to phase separate as ionic strength of the solution increases. Red and blue dots represent the positively and negatively charged Na+ and Clions, respectively. Green lines represent his-FUS LC chains. Yellow bubbles represent regions of FUS LC self-interaction, such as π - π stacking and hydrophobic interactions. (B) Representative confocal maximum-intensity projections of LDs demonstrating uniform binding (no phase separation, left column), emerging phase separation (center column), and full phase separation (right column). The red channel depicts the lipid channel (DHPE-Texas Red) and the green channel depicts the his-FUS LC protein channel (ATTO-488). Emerging phase separation domains were defined by four or more individual resolvable protein-depleted or protein-rich domains. Scale bars, 5 µm. (C) Phase separation diagram mapping the percentage of LDs with uniform protein binding (black), emerging phase separation (gray), and full phase separation (green) under protein concentrations ranging from 1 to 3 µM and NaCl concentrations ranging from 50 to 250 mM in 25 mM HEPES (pH 7.4). Data represent the mean ± SE from >330 LDs from 15 or more fields of view per condition in 3 independent experiments. LD monolayer interfaces were composed of 83 mol % DOPC, 15 mol % DGS-NTA(Ni), 2 mol % Biotinyl Cap PE, and 0.1 mol % Texas Red-DHPE. To see this figure in color, go online.

of Caenorhabditis elegans (46). LAF-1 RGG is an arginine/glycine rich disordered protein that undergoes electrostatically driven LLPS in solution (46). Indeed, when we incubated C-terminally His-tagged RGG (his-RGG) with LDs containing DGS-NTA(Ni), we observed LLPS that appeared morphologically similar to that of his-FUS LC (Fig. 5 A). When we mapped the phase behavior of his-RGG on the LD surface as a function of ionic strength, we observed a decrease in the number of LDs with LLPS on their surfaces as NaCl concentration increased (Fig. 5, B and C). This observation is opposite of the trend that we observed with FUS LC, owing to the difference in the amino acid content of the RGG domain. Specifically, RGG is rich in arginine and glycine residues, so a combination of electrostatic and hydrophobic interactions, such as charge-charge, cation- π , dipole-dipole, and π - π stacking, mediate protein condensation. As salt concentration increases, electrostatic forces weaken due to charge screening, and the hydrophobic effect is enhanced (47). Thus, condensation that is dominated by electrostatic interactions, such as for RGG, is less favorable at higher salt concentrations, while condensation that is dominated by hydrophobic interactions, as is the case for FUS LC, becomes more favorable as ionic strength increases. The alignment of our results with previously observed trends for FUS LC (9) and RGG (48) demonstrates that LLPS on the LD surface is likely driven by the same intermolecular interactions that govern the formation of the respective biomolecular condensates in solution. Furthermore, LAF-1 RGG LLPS occurred on LDs at a concentration of 3 μ M, under which no droplet formation was observed in solution (Fig. S4); 12 μ M is the reported saturation concentration of LAF-1 at room temperature (49). Collectively, these findings suggest that, similar to bilayer membranes, synthetic

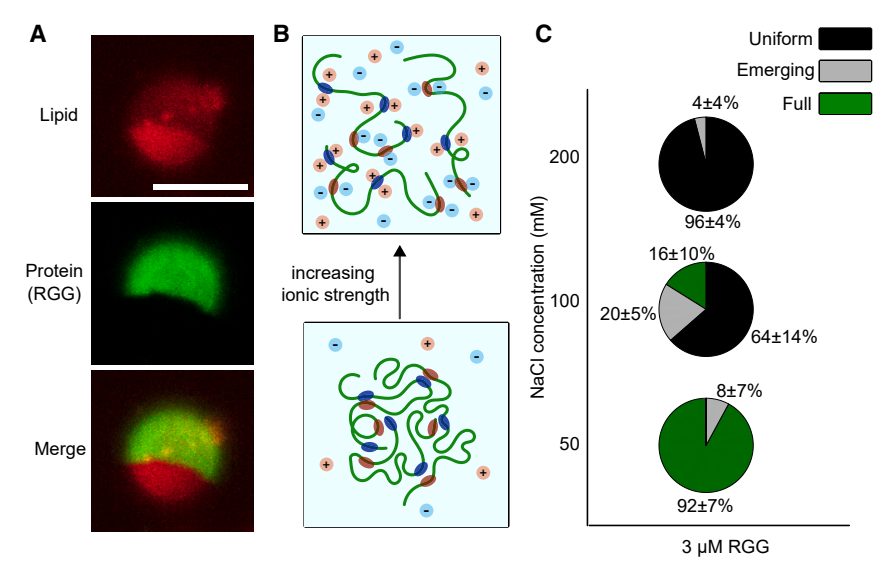


FIGURE 5 LLPS of his-RGG is screened by increasing ionic strength. (A) Representative maximum intensity projections of 3 µM ATTO-488-labeled his-RGG phase separation on DGS-NTA(Ni)-containing LDs. Scale bar, 5 μ m. (B) Schematic depicting the predicted tendency of his-RGG condensates to dissolve upon increasing ionic strength of the solution. Light red and blue circles in solution represent positively and negatively charged Na+ and Cl- ions in solution, respectively. Green lines represent Atto488-labeled his-RGG protein chains. Dark red and blue ovals attached to his-RGG represent regions of RGG that participate in electrostatic self-interactions. (C) Phase separation diagram mapping the percentage of LDs with uniform binding (black), emerging phase separation (gray), and full phase separation (green) at 3 μ M his-RGG and NaCl concentrations ranging from 50 to 200 mM NaCl in 25 mM HEPES (pH 7.4). Data represent the mean \pm SE from >220 LDs from 15 or more fields of view per condition in 3 independent

experiments. LD monolayer interfaces were composed of 83 mol % DOPC, 15 mol % DGS-NTA(Ni), 2 mol % Biotinyl Cap PE, and 0.1 mol % Texas Red-DHPE. To see this figure in color, go online.

LDs can serve as nucleating surfaces for two-dimensional protein phase separation, although the ability to nucleate LLPS appears to be protein dependent (Fig. S3).

Condensation of his-FUS LC and his-RGG on cellderived LDs

The surface of cellular LDs differs from our synthetic LDs in lipid composition, surface tension, and in the presence of surface proteins that bind to LDs within cells. For example, the reported surface tension of cellular LDs isolated from mammalian cells is ~ 3.5 mN/m (50), compared with the minimal surface tension of synthetic LDs made with PC (\sim 0.5 mN/m) (51), and perilipin proteins (PLIN1-5), lipases, acyltransferases, and acyl-coA synthetases densely populate the LD surface (52). Therefore, we wondered if protein phase separation was also possible on the surfaces of cellular LDs. To address this question, we isolated LDs from oleate-fed RPE cells (Fig. 6 A, panels 1-3) and examined exogenous protein binding to these cell-derived LDs. To enable binding of his-FUS LC and RGG proteins to the cell-derived LD, we incorporated DGS-NTA(Ni) into the LD surface. Before investigating protein binding and condensation, we attempted to visualize whether exogenous lipids could successfully be incorporated onto the cell-derived LD surface through addition of Texas Red-DHPE to cell-derived LDs. When DGS-NTA(Ni) and Texas Red-DHPE were added simultaneously to cell-derived LDs at 14 and 1.4 μM concentrations, respectively, a fluorescent ring was clearly observed at the LD surface (Fig. 6 A, panel 4). This observation confirms that exogenous lipids were successfully incorporated into the phospholipid monolayer of our cell-derived LDs. We also confirmed binding of his-FUS LC and RGG proteins to the cell-derived LDs, suggesting successful incorporation of DGS-NTA(Ni) (Fig. 6 *B*).

Upon incorporation of DGS-NTA(Ni) and subsequent addition of protein to cell-derived LDs, we observed binding and protein enrichment of FUS LC or RGG, individually, on the cell-derived LD surface, which looked similar to our previous observations of protein phase separation on synthetic LDs (compare Figs. 2 B and 6 B). To test whether the enrichment on cell-derived LDs was an effect of uneven DGS-NTA(Ni) incorporation on the LD surface or protein condensation, we compared cell-derived LDs with FUS LC or RGG to cell-derived LDs with His-tagged mCherry, a well-structured fluorescent protein that does not undergo protein phase separation. When mCherry bound to our cell-derived LDs, we observed uniform binding to the surface of the majority of LDs, suggesting that the regions of FUS LC and RGG enrichment were an effect of the proteins' ability to self-interact, rather than a feature of the lipid distribution (Fig. 6 B). Notably, protein-enriched regions were observed with around fivefold greater frequency on the surfaces of LDs exposed to FUS LC or RGG, compared with mCherry, suggesting that these regions were the result of LLPS, rather than nonspecific protein aggregation (Student's t-test, p values of 0.0037 and 0.0019, respectively) (Figs. 6 C and S5). In addition, we calculated the average partition coefficient for each protein on cell-derived LDs. We defined the partition coefficient as the ratio of the background-subtracted intensities of the maximum peak to the minimum peak along a line profile through the LD. The line profile was drawn through regions of high and low intensity, if present, or across any location on the LD if binding was visibly uniform. The resulting average partition coefficients for FUS LC and RGG were about twofold greater than that of mCherry on cell-derived LDs (Student's t-test, p values of 0.0270 and 0.0003, respectively) (Fig. 6

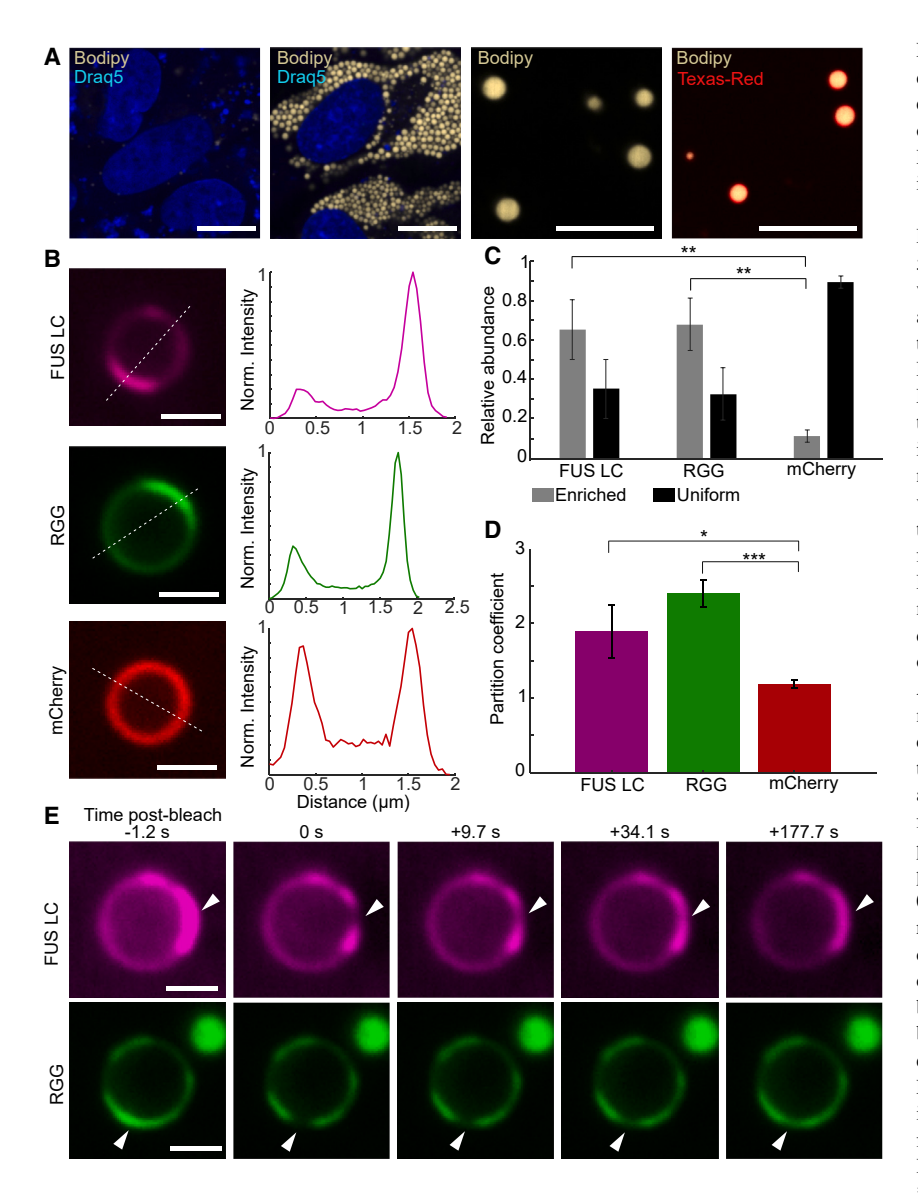


FIGURE 6 LLPS of FUS LC and RGG on cellderived LDs. (A) From left to right, RPE cells without exogenously added BSA-oleate, RPE cells with 1 mM of exogenously added BSA-oleate, LDs isolated from RPE cells fed with 1 mM exogenous BSA-oleate, and isolated LDs doped with 14 µM DGS-NTA(Ni) and 1.4 μM Texas Red-DHPE. Cells were stained with Drag5 for nuclei (blue) and the neutral lipid dye Bodipy 505/515 for LDs (beige). Cell-derived LDs were stained with Bodipy 505/515. Scale bars, 10 μm (for cell images) and 5 µm (for isolated LD images). (B) Representative images of cell-derived LDs doped with 60 μM DGS-NTA(Ni) in the presence of 5 μ M Atto647-FUS LC, Atto488-RGG, or mCherry. Line profiles depict intensity values across the dashed line in the corresponding image. Line profiles were background subtracted and normalized to the minimum and maximum intensity values. Scale bars, 1 µm. (C) Quantification of the relative abundance of uniformly bound and enriched protein for FUS LC, RGG, and mCherry on cell-derived LDs. Data are mean + SD across n = 3 independent experiments, with at least 28 LDs analyzed per replicate. Student's t test p-values are 0.0037 and 0.0019 for FUS LC or RGG compared to mCherry, respectively. (D) Average partition coefficient of FUS LC, RGG, and mCherry for the LDs analyzed in (C). Partition coefficients were calculated as the ratio of background-subtracted intensity values between the enriched phase and dilute phase, if present, or across two regions of uniform binding. Data are mean + SD across n = 3 independent experiments, with at least 28 LDs analyzed per replicate. Student's t test p-values are 0.0270 and 0.0003 between FUS LC or RGG compared to mCherry, respectively). (E) Time series images of fluorescence recovery of FUS LC- and RGG-enriched regions on the cell-derived LD surface. Timestamps indicate the postbleach time. Images are representative of recovery behavior observed on at least three separate LDs for each protein. Scale bars, 1 µm. Experiments for FUS LC and mCherry on cell-derived LDs were conducted in 25 mM HEPES, 150 mM NaCl (pH 7.4). Experiments for RGG on cell-derived LDs were conducted in 25 mM HEPES, 137 mM NaCl (pH 7.4). For all statistics, p < 0.05, p < 0.01, p < 0.001. To see this figure in color, go online.

D). Together, these data strengthened our hypothesis that the regions of FUS LC and RGG enrichment occurred because the proteins self-interact and condense.

We next asked whether regions of FUS LC and RGG enrichment on the surfaces of cell-derived LDs behaved in a liquid-like manner. To assess the mobility of the proteinenriched regions, we bleached small sections of them and observed the fluorescence recovery over time. Within the bleached regions, both FUS LC and RGG visibly recovered within 180 s, suggesting that protein within the enriched phase is mobile (Fig. 6 E). It is possible, in principle, that NiNTA-containing protein condensates assemble in solution and then associate with the LD surface, because after washing, residual NiNTA causes some protein assembly (Fig. S6 A). However, the inability of FUS LC condensates touching an LD surface to wet the LD and form two-dimensional phase separated patches (Fig. S6 C), and no observation of fusion events between aggregates and the LD surface in the presence of NiNTA, suggests that this is highly unlikely. Thus, our observations suggest that dynamic protein condensates can form on the surfaces of complex, cellderived LDs, as well as artificially prepared LDs.

DISCUSSION

We have demonstrated that protein phase separation can occur on the surfaces of LDs, which are ubiquitous intracellular lipid substrates. Similar to what has been observed previously with lipid bilayers, LLPS occurs on the surfaces of LDs at substantially lower protein concentrations than those required for LLPS in solution. A growing body of recent work has shown that interactions with membranes are an

important mechanism by which cells can control LLPS (4– 6). Specifically, by restricting diffusion of proteins to a twodimensional surface, membranes can reduce the critical concentration necessary for protein phase separation (7). Here, we have shown that the phospholipid monolayer of LDs can perform this same function, though not for all proteins, which suggests LDs as another candidate lipid substrate for intracellular nucleation of LLPS in addition to phospholipid membranes. The observed phase separation demonstrates several characteristics of a liquid, including the merging and re-rounding of distinct protein-rich or protein-depleted domains and rapid molecular recovery. This liquid-like behavior suggests that protein condensates on the surfaces of LDs could react quickly to changes in the intracellular environment (7) and organize proteins to catalyze important cellular processes (5).

The LLPS we observed on the surface of LDs was dependent on the protein concentration and ionic strength of the solution. Specifically, when we increased the NaCl concentration from 50 to 250 mM, we observed a sharp increase in the number of LDs on which FUS LC underwent LLPS. In contrast, under the same solution conditions, we observed a sharp decrease in the number of LDs on which LAF-1 RGG underwent LLPS. Increasing the ionic strength of the solution increases the relative strength of the hydrophobic interactions that drive the condensation of FUS LC, while screening the electrostatic interactions critical for LAF-1 RGG condensation. The agreement between these results and the phase behavior previously characterized for FUS LC (9) and LAF-1 RGG (48) in solution indicates that proximity to the LD surface does not alter or interfere with the molecular interactions driving phase separation of FUS LC and LAF-1 RGG. Further, our observation of FUS LC and RGG LLPS on the surface of LDs isolated from cells shows that, despite the increased complexity of the LD proteome and lipidome compared with reconstituted synthetic LDs, protein LLPS on the lipid monolayer of cell-derived LDs is possible. Cell-derived LDs differ in surface tension from both synthetic LDs and bilayer membranes (50,51). How the LD surface tension influences the phase separation behavior of a protein, especially when bound with a more physiological binding mechanism like an amphipathic helix or helical hydrophobic domain (53), poses an important question for future biophysical studies.

It is well established that LD-associated proteins play important roles in cellular metabolism, including the synthesis and lipolysis of TAGs and protection against cellular stress (54). However, our knowledge and characterization of the structure of many LD-associated proteins remains largely unexplored (55), and many fundamental processes in LD biology, including the process of LD biogenesis and mechanisms of protein targeting to LDs remain unclear (56). For example, LD formation begins with TAG synthesis by the enzymes DGAT1 and DGAT2 and accumulation of TAGs between the leaflets of the ER membrane to form an

oil lens (57). Whether cells have specific sites for lens nucleation and how these sites are determined remains unclear. Similarly, whether and how proteins are involved in determining the direction of LD budding into the cytosol and the scission of LDs from the ER remains to be determined (56).

Could the LLPS of lipid-droplet binding proteins with IDRs play a role in these unanswered questions in LD biology? Building on our results, examining the intersection between the fields of LD cell biology and biophysics could yield candidate proteins for this phenomenon. Indeed, the native LDbinding protein Cidec was recently found to undergo condensation at LD contact sites despite the apparent lack of an IDR, and its ability to phase-separate was found to be essential for Cidec to perform its function of promoting LD fusion (20). However, Cidec condensation was distinctly gel-like and condensation on other regions of the LD surface was not observed, even when Cidec was bound to the LD at sufficient concentrations (20). Further screening for LD-binding proteins with IDRs could yield proteins that behave as we have observed here with model phase-separating proteins, namely a liquid-like condensation that can spontaneously occur on free LDs, even in the absence of molecular crowders. As a further suggestion that LLPS could play a role in LD biology, local membrane curvature and protein clustering, both of which can be induced by LLPS on membranes (11,16,58), are also hypothesized to play a role in organizing the early assembly of LDs (56). Whether LLPS plays a role in these processes remains to be determined. As exploration of the LD proteome continues, the ability of LDs to nucleate phase separation could shed light on multiple facets of LD biology.

CONCLUSION

In this work, we used synthetic and cell-derived LDs to investigate the ability of lipid monolayers to serve as templates for phase separation of model LLPS proteins FUS LC and LAF-1 RGG. We find that LDs can serve as substrates for protein phase separation, although the ability of the monolayer to nucleate phase separation at lower concentrations than on a bilayer or in solution varies based on the model protein. Our experiments indicate that the nature of the intermolecular interactions driving phase separation of these model proteins (e.g., electrostatics, hydrophobic interactions) are not altered by the lipid monolayer, and that the two-dimensional condensates remain relatively liquid-like. Our observation of protein phase separation on cell-derived LDs suggests that, despite the increased complexity of the cellular LD surface, proteins can still retain properties, such as mobility and multivalent interactions, which are necessary for phase separation. The formation of distinct protein condensates on the monolayer of LDs rather than a contact site between two LD has not, to our knowledge, been reported, and opens new paths in the understanding of how proteins can organize on the LD surface.

SUPPORTING MATERIAL

Supporting material can be found online at https://doi.org/10.1016/j.bpj. 2024.03.015.

AUTHOR CONTRIBUTIONS

A.K., J.C.S., and S.H.P. designed the study. A.K. performed all experiments and analyzed all data. J.P.K.B. and D.W.T. worked with A.K. on electron microscopy experiments. F.Y. expressed, purified, and characterized the FUS LC and RGG proteins utilized in this study. L.W. and E.M.L. expressed, purified, and characterized the his-clathrin protein utilized in this study. J.C.S. and S.H.P. conceived and supervised the study. A.K., J.C.S., and S.H.P. wrote the manuscript with input and comments from all authors.

ACKNOWLEDGMENTS

A.K. acknowledges financial support from the National Science Foundation Graduate Research Fellowship Program under grant no. DGE 2137420, the UT Austin Provost's Graduate Excellence Fellowship, and the UT Austin Thrust 2000 John E. Kasch Endowed Graduate Fellowship in Engineering. F.Y. acknowledges support from The University of Texas at Austin, Graduate School Continuing Fellowship 2022-2023. J.C.S. acknowledges financial support from the NIH R35GM139531 and Welch Foundation F-2047. S.H.P. acknowledges financial support from the National Science Foundation (no. 2146549) and Welch Foundation F-2008-20220331. The content is solely the responsibility of the authors and does not necessarily represent the official views of the funding agencies.

DECLARATION OF INTERESTS

The authors declare no competing interests.

REFERENCES

- Alberti, S., A. Gladfelter, and T. Mittag. 2019. Considerations and Challenges in Studying Liquid-Liquid Phase Separation and Biomolecular Condensates. *Cell.* 176:419

 –434.
- 2. Shin, Y., and C. P. Brangwynne. 2017. Liquid phase condensation in cell physiology and disease. *Science*. 357, eaaf4382.
- Boeynaems, S., S. Alberti, ..., M. Fuxreiter. 2018. Protein Phase Separation: A New Phase in Cell Biology. Trends Cell Biol. 28:420–435.
- Snead, W. T., A. P. Jalihal, ..., A. S. Gladfelter. 2022. Membrane surfaces regulate assembly of ribonucleoprotein condensates. *Nat. Cell Biol.* 24:461–470.
- Day, K. J., G. Kago, ..., J. C. Stachowiak. 2021. Liquid-like protein interactions catalyse assembly of endocytic vesicles. *Nat. Cell Biol.* 23:366–376.
- Chatterjee, S., D. Maltseva, ..., S. H. Parekh. 2022. Lipid-driven condensation and interfacial ordering of FUS. Sci. Adv. 8, eabm7528.
- Snead, W. T., and A. S. Gladfelter. 2019. The Control Centers of Biomolecular Phase Separation: How Membrane Surfaces, PTMs, and Active Processes Regulate Condensation. *Mol. Cell.* 76:295–305.
- 8. Zhang, H., S. Elbaum-Garfinkle, ..., A. S. Gladfelter. 2015. RNA controls PolyQ protein phase transitions. *Mol. Cell.* 60:220–230.
- Burke, K. A., A. M. Janke, ..., N. L. Fawzi. 2015. Residue-by-Residue View of In Vitro FUS Granules that Bind the C-Terminal Domain of RNA Polymerase II. *Mol. Cell*. 60:231–241.
- van Meer, G., D. R. Voelker, and G. W. Feigenson. 2008. Membrane lipids: where they are and how they behave. *Nat. Rev. Mol. Cell Biol*. 9:112–124.

- Yuan, F., H. Alimohamadi, ..., J. C. Stachowiak. 2021. Membrane bending by protein phase separation. *Proc. Natl. Acad. Sci. USA*. 118, e2017435118.
- 12. Wang, Y., C. Zhang, ..., C. Wu. 2021. LIMD1 phase separation contributes to cellular mechanics and durotaxis by regulating focal adhesion dynamics in response to force. *Dev. Cell.* 56:1313–1325.e7.
- Banjade, S., and M. K. Rosen. 2014. Phase transitions of multivalent proteins can promote clustering of membrane receptors. *Elife*. 3, e04123.
- 14. Milovanovic, D., Y. Wu, ..., P. De Camilli. 2018. A liquid phase of synapsin and lipid vesicles. *Science*. 361:604–607.
- Zeng, M., X. Chen, ..., M. Zhang. 2018. Reconstituted Postsynaptic Density as a Molecular Platform for Understanding Synapse Formation and Plasticity. *Cell*. 174:1172–1187.e16.
- Ramella, M., L. M. Ribolla, and I. de Curtis. 2022. Liquid–Liquid Phase Separation at the Plasma Membrane–Cytosol Interface: Common Players in Adhesion, Motility, and Synaptic Function. *J. Mol. Biol.* 434, 167228.
- Su, X., J. A. Ditlev, ..., R. D. Vale. 2016. Phase separation of signaling molecules promotes T cell receptor signal transduction. *Science*. 352:595–599.
- Farmer, B. C., A. E. Walsh, ..., L. A. Johnson. 2020. Lipid Droplets in Neurodegenerative Disorders. Front. Neurosci. 14:742.
- Yang, L., Y. Ding, ..., P. Liu. 2012. The proteomics of lipid droplets: structure, dynamics, and functions of the organelle conserved from bacteria to humans. J. Lipid Res. 53:1245–1253.
- Lyu, X., J. Wang, ..., P. Li. 2021. A gel-like condensation of Cidec generates lipid-permeable plates for lipid droplet fusion. *Dev. Cell*. 56:2592–2606.e7.
- Zeno, W. F., J. B. Hochfelder, ..., J. C. Stachowiak. 2021. Clathrin senses membrane curvature. *Biophys. J.* 120:818–828.
- Stachowiak, J. C., E. M. Schmid, ..., C. C. Hayden. 2012. Membrane bending by protein-protein crowding. *Nat. Cell Biol.* 14:944–949.
- Punjani, A., J. L. Rubinstein, ..., M. A. Brubaker. 2017. cryoSPARC: algorithms for rapid unsupervised cryo-EM structure determination. *Nat. Methods.* 14:290–296.
- Peterson, C. W. H., K. K. Deol, ..., J. A. Olzmann. 2021. Optimized protocol for the identification of lipid droplet proteomes using proximity labeling proteomics in cultured human cells. STAR Protoc. 2, 100579.
- Momin, N., S. Lee, ..., D. Y. Sasaki. 2015. Designing lipids for selective partitioning into liquid ordered membrane domains. *Soft Matter*. 11:3241–3250.
- Wang, Y., X.-M. Zhou, ..., P. Liu. 2016. Construction of Nanodroplet/ Adiposome and Artificial Lipid Droplets. ACS Nano. 10:3312–3322.
- Komaiko, J., A. Sastrosubroto, and D. J. McClements. 2015. Formation
 of Oil-in-Water Emulsions from Natural Emulsifiers Using Spontaneous Emulsification: Sunflower Phospholipids. *J. Agric. Food Chem.*63:10078–10088.
- Regan, D., J. Williams, ..., W. Langbein. 2019. Lipid Bilayer Thickness Measured by Quantitative DIC Reveals Phase Transitions and Effects of Substrate Hydrophilicity. *Langmuir*. 35:13805–13814.
- Gallová, J., D. Uhríková, ..., P. Balgavý. 2004. Effect of cholesterol on the bilayer thickness in unilamellar extruded DLPC and DOPC liposomes: SANS contrast variation study. *Gen. Physiol. Biophys.* 23:113–128.
- Stribny, J., and R. Schneiter. 2023. Binding of perilipin 3 to membranes containing diacylglycerol is mediated by conserved residues within its PAT domain. J. Biol. Chem. 299, 105384.
- Nye, J. A., and J. T. Groves. 2008. Kinetic Control of Histidine-Tagged Protein Surface Density on Supported Lipid Bilayers. *Langmuir*. 24:4145–4149.
- Giménez-Andrés, M., T. Emeršič, ..., A. Čopič. 2021. Exceptional stability of a perilipin on lipid droplets depends on its polar residues, suggesting multimeric assembly. *Elife*. 10, e61401.

- 33. Caillon, L., V. Nieto, ..., A. R. Thiam. 2020. Triacylglycerols sequester monotopic membrane proteins to lipid droplets. Nat. Commun. 11:3944.
- 34. Wilfling, F., H. Wang, ..., T. C. Walther. 2013. Triacylglycerol Synthesis Enzymes Mediate Lipid Droplet Growth by Relocalizing from the ER to Lipid Droplets. Dev. Cell. 24:384-399.
- 35. Shen, W.-J., S. Patel, ..., F. B. Kraemer. 2009. Functional interaction of hormone-sensitive lipase and perilipin in lipolysis. J. Lipid Res. 50:2306-2313.
- 36. Prévost, C., M. E. Sharp, ..., T. C. Walther. 2018. Mechanism and Determinants of Amphipathic Helix-Containing Protein Targeting to Lipid Droplets. Dev. Cell. 44:73-86.e4.
- 37. Chorlay, A., and A. R. Thiam. 2020. Neutral lipids regulate amphipathic helix affinity for model lipid droplets. J. Cell Biol. 219, e201907099.
- 38. García-Sáez, A. J., S. Chiantia, and P. Schwille. 2007. Effect of line tension on the lateral organization of lipid membranes. J. Biol. Chem. 282:33537-33544.
- 39. Usery, R. D., T. A. Enoki, ..., G. W. Feigenson. 2017. Line Tension Controls Liquid-Disordered + Liquid-Ordered Domain Size Transition in Lipid Bilayers. Biophys. J. 112:1431-1443.
- 40. Morris, K. L., J. R. Jones, ..., C. J. Smith. 2019. Cryo-EM of multiple cage architectures reveals a universal mode of clathrin self-assembly. Nat. Struct. Mol. Biol. 26:890–898.
- 41. Zacharias, D. A., J. D. Violin, ..., R. Y. Tsien. 2002. Partitioning of Lipid-Modified Monomeric GFPs into Membrane Microdomains of Live Cells. Science. 296:913-916.
- 42. von Stetten, D., M. Noirclerc-Savoye, ..., A. Royant. 2012. Structure of a fluorescent protein from Aequorea victoria bearing the obligatemonomer mutation A206K. Acta Crystallogr. Sect. F: Struct. Biol. Cryst. Commun. 68:878-882.
- 43. Myatt, D. P., L. Hatter, ..., L. A. Clifton. 2017. Monomeric green fluorescent protein as a protein standard for small angle scattering. Biomed. *Spectrosc. Imag.* 6:123–134.
- 44. Sarkar, P., and A. Chattopadhyay. 2020. Exploring Membrane Lipid and Protein Diffusion by FRAP. In Analysis of Membrane Lipids. R. Prasad and A. Singh, eds Springer US, pp. 119-141.
- 45. Murthy, A. C., G. L. Dignon, ..., N. L. Fawzi, 2019. Molecular interactions underlying liquid-liquid phase separation of the FUS lowcomplexity domain. Nat. Struct. Mol. Biol. 26:637-648.

- 46. Elbaum-Garfinkle, S., Y. Kim, ..., C. P. Brangwynne. 2015. The disordered P granule protein LAF-1 drives phase separation into droplets with tunable viscosity and dynamics. Proc. Natl. Acad. Sci. USA. 112:7189-7194.
- 47. Krainer, G., T. J. Welsh, ..., T. P. J. Knowles. 2021. Reentrant liquid condensate phase of proteins is stabilized by hydrophobic and nonionic interactions. Nat. Commun. 12:1085.
- 48. Wei, M.-T., S. Elbaum-Garfinkle, ..., C. P. Brangwynne. 2017. Phase behaviour of disordered proteins underlying low density and high permeability of liquid organelles. Nat. Chem. 9:1118-1125.
- 49. Schuster, B. S., E. H. Reed, ..., D. A. Hammer. 2018. Controllable protein phase separation and modular recruitment to form responsive membraneless organelles. Nat. Commun. 9:2985.
- 50. Ben M'barek, K., D. Ajjaji, ..., A. R. Thiam. 2017. ER Membrane Phospholipids and Surface Tension Control Cellular Lipid Droplet Formation. Dev. Cell. 41:591-604.e7.
- 51. Chorlay, A., L. Monticelli, ..., A. Rachid Thiam. 2019. Membrane Asymmetry Imposes Directionality on Lipid Droplet Emergence from the ER. Dev. Cell. 50:25-42.e7.
- 52. Bersuker, K., and J. A. Olzmann. 2018. In Close Proximity: The Lipid Droplet Proteome and Crosstalk with the Endoplasmic Reticulum. Contact (Thousand Oaks). https://doi.org/10.1177/2515256418768996.
- 53. Thiam, A. R., and I. Dugail. 2019. Lipid droplet-membrane contact sites - from protein binding to function. J. Cell Sci. 132:jcs230169.
- 54. Jarc, E., and T. Petan. 2019. Lipid Droplets and the Management of Cellular Stress. Yale J. Biol. Med. 92:435-452.
- 55. Redwan, E. M., S. A. Alkarim, ..., V. N. Uversky. 2020. Disorder in milk proteins: adipophilin and TIP47, important constituents of the milk fat globule membrane. J. Biomol. Struct. Dyn. 38:1214-1229.
- 56. Walther, T. C., J. Chung, and R. V. Farese. 2017. Lipid Droplet Biogenesis. Annu. Rev. Cell Dev. Biol. 33:491-510.
- 57. Olzmann, J. A., and P. Carvalho. 2019. Dynamics and functions of lipid droplets. Nat. Rev. Mol. Cell Biol. 20:137-155.
- 58. Case, L. B., J. A. Ditley, and M. K. Rosen. 2019. Regulation of Transmembrane Signaling by Phase Separation. Annu. Rev. Biophys. 48:465-494.